ADVANCED FUNCTIONAL MATERIALS
www.afm-journal.de

# Mechanically Tough Micellar Cubic Liquid-Crystalline Polymer Electrolytes for Electromechanical Actuators

*Masafumi Yoshio,* Che-Hao Wu, and Chengyang Liu*

**This study presents a novel micellar cubic ionic liquid-crystalline polymer electrolyte, featuring an alignment-free spherical structure with unimpeded 3D ionic pathways, aimed at enhancing the performance of an ionic electroactive polymer actuator. The development involved creating a mechanically tough and high ion-conductive cubic polymer film through the self-assembly of a wedge-shaped vinyl imidazolium salt and an imidazolium ionic liquid, followed by in situ photopolymerization. The 300 µm-thick-trilayer films, consisting of the cubic polymer electrolyte sandwiched between poly(3,4-ethylenedioxythiophene)-poly(styrenesulfonate) (PEDOT:PSS) electrodes, exhibit remarkable capabilities. These include bearing substantial loads of 4 g with a high blocking force under a DC voltage of 2 V, achieving a high bending strain of 0.63% under a low input voltage (±2 V, 0.1 Hz), and boasting a maximum response frequency of 70 Hz. These properties position the material for potential applications in soft robots and tactile sensing devices.**

## 1. Introduction

Ionic electroactive polymer (iEAP) actuators have garnered significant attention as practical tools for energy storage and transduction. These actuators offer remarkable advantages, including low operating voltages, high deformability, controllable generation force, and lightweight properties, making them ideal for the development of soft electronic devices.[1–3] While many high-performance iEAP actuators can achieve substantial bending deformation using functionalized materials rich in ionic liquids, they often overlook the aspect of force generation.[4–8] To create iEAP actuators capable of both high deformation and force generation, it is crucial to design the nanoscale morphologies within the ionic polymer electrolytes to effectively control mechanical characteristics and enhance ion transport. Despite the availability of various nanostructured polymer electrolytes that perform well in iEAP actuators,[9,10] addressing issues related to the lack of mechanical properties in physically crosslinked polymer electrolytes and the undesired plasticization from excessive ionic liquids remains a challenge yet to be fully resolved.

This paper discusses the potential of intuitive alignment-free micellar cubic structures with spherical symmetry ($Cub_M$), comprising hydrophobic spheres encased in hydrophilic shells, as a promising solution for enabling efficient ion migration within a mechanically robust polymer membrane. This ion migration in the micellar cubic structure occurs by traversing the spherical surface with positive interfacial curvature, which would provide a high-efficiency ion transporting for iEAP actuators.

The creation of 3D periodic cubic structures within polymer electrolytes is of paramount importance.[11–13] These periodic cubic structures emerge from the microphase separation of amphiphilic molecules, dividing space into two interwoven and continuous networks. Within these periodic nanostructures, free ions can diffuse in a 3D open space unimpeded by boundary layers. Namely, the ion-conductive pathways in a 3D cubic structure exhibit significantly lower tortuosity compared to their counterparts in inner conductive columnar and layer structures.[14–17] Additionally, cubic lattices offer higher viscoelastic behavior, contributing to enhanced modulus.[11,18] Among the various periodic cubic structures, $Cub_M$ structures are the most common occurrence in various lyotropic systems.[19,20] We expect that the polymer electrolyte, in combination with its viscoelasticity cubic structure and alignment-free ion pathways, will pave the way for the development of a new generation of mechanically tough iEAP actuators. However, strategies to construct such normal $Cub_M$ structures through self-assembled block copolymers often necessitate a careful investigation of their complex thermodynamic behavior and the selection of suitable functional monomers.[21–24]

M. Yoshio, C.-H. Wu, C. Liu
Research Center for Macromolecules & Biomaterials
National Institute for Materials Science
1-2-1 Sengen, Tsukuba, Ibaraki 305-0047, Japan
E-mail: YOSHIO.Masafumi@nims.go.jp
M. Yoshio, C.-H. Wu, C. Liu
Graduate School of Chemical Sciences and Engineering
Hokkaido University
Kita 13, Nishi 8, Kita-ku, Sapporo, Hokkaido 060–8628, Japan
M. Yoshio
Japan Science and Technology Agency
PRESTO, 4-1-8 Honcho, Kawaguchi, Saitama 332-0012, Japan

The ORCID identification number(s) for the author(s) of this article can be found under https://doi.org/10.1002/adfm.202314087



**DOI: 10.1002/adfm.202314087**

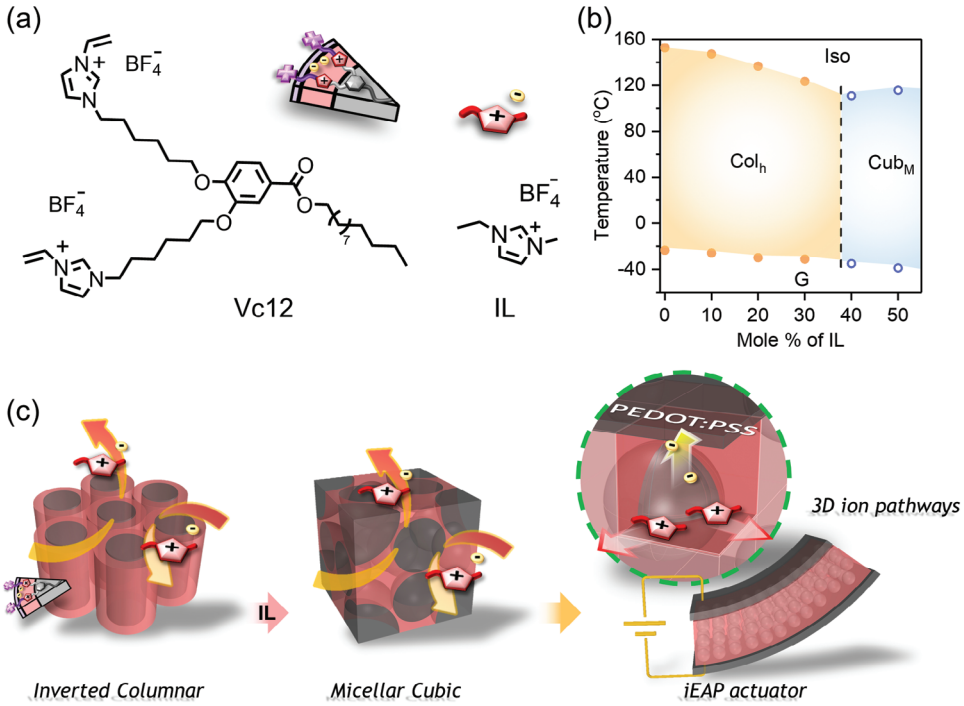


**Figure 1.** a) Molecular structure of a taper-shaped ionic LC monomer Vc12 and an ionic liquid [Emim][$BF_4$] (IL). b) Phase-transition temperatures of the binary mixtures of Vc12 and IL as a function of the mole % of IL. The temperatures were determined through the heating scan in the DSC measurements. G, $Col_h$, $Cub_M$, and Iso represent the glassy, hexagonal columnar, micellar cubic, and isotropic liquid phases, respectively. c) The schematic depicts the transformation of the $Col_h$ phase to the $Cub_M$ phase with the addition of IL, followed by photo-polymerization to produce the polymer film. The iEAP actuator was constructed using the $Cub_M$ LC membrane sandwiched between PEDOT:PSS electrodes, where the LC electrolyte possesses an alignment-free spherical structure with unimpeded 3D ionic pathways.

In response to the immediate challenge in the structural design of the new iEAP actuator, we identified photocured ionic liquid-crystalline (LC) membranes with nanoscale ion channels as highly favorable candidates. By harnessing the influence of molecular shape and interactions on self-assembled ionic liquid crystals, we could effectively control resulting morphologies and subsequently polymerize them to obtain free-standing LC membranes. We have previously reported several nanostructured LC membrane-based actuators with hexagonally packed columnar ($Col_h$)[25] and layered (Sm) morphologies,[26] showcasing exceptional bendability even with low ionic liquid content (<15 wt%). However, these structures necessitate intricate alignment treatment of 1D or 2D pathways to achieve optimal performance.

Furthermore, we introduced an innovative design concept for a 3D $Col_h$ structure, featuring ionophobic cylinder surrounded by ionic shells.[27] This concept establishes a substitution scheme resembling a cubic structure, facilitated by the formation of interconnected ionic domains between each LC column. Nonetheless, the orientation of these LC columns in the membrane has a relatively minor impact on their mechanical property and ionic conductivity.

In this study, we introduce an innovative photocured $Cub_M$ LC polymer electrolyte membrane, composed of a polymerizable imidazolium liquid crystal and an ionic liquid (**Figure 1**), expertly sandwiched between PEDOT:PSS electrodes. This pioneering design empowers the new generation of iEAP actuators to achieve a remarkable ability to bear substantial loads of 4 g with a high blocking force and a high bending strain of 0.63% under a low input voltage (±2 V, 0.1 Hz). Remarkably, this exceptional performance is consistently maintained during stable operation in ambient conditions for over 10,000 cycles. To the best of our knowledge, this study marks the first demonstration of a mechanically tough thermotropic $Cub_M$ LC membrane electrolyte successfully applied in electromechanical transduction devices.

## 2. Results and Discussion

We have designed a novel taper-shaped ionic LC monomer (Vc12) to create a well-defined thermotropic $Cub_M$ LC structure. Vc12 consists of two vinyl imidazolium groups and a single alkyl chain (Figure 1a). The details of synthetic procedure and its nuclear magnetic resonance (NMR) spectra were recorded in the Supporting Information (Figures S1 and S2, Supporting Information). The alkyl chain plays a key role in stabilizing the LC mesophase.[27] The combination of Vc12 and IL results in a broad temperature range exhibiting $Col_h$ and $Cub_M$ phases with interconnected polar domains (Figure 1b). Vc12 exhibits a $Col_h$ phase between –23.5 and 152.6 °C upon heating (**Figure 2**a). The polarizing optical microscopy (POM) reveals a fan texture with some black regions (Figure 2b, upper panel), indicating a combined texture resulting from both random and vertically oriented LC columns. Small-angle X-ray scattering (SAXS) pattern displays three distinct peaks at $q$ = 1.29, 2.24, and 2.59 $nm^{-1}$, corresponding to the (100), (110), and (200) diffractions of the $Col_h$

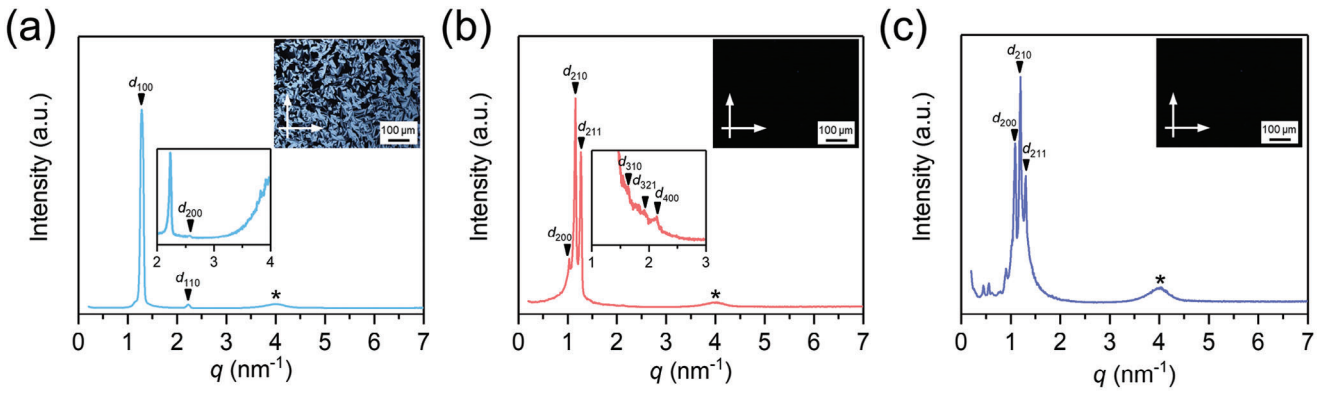


**Figure 2.** SAXS profiles for a) Vc12, b) Vc12/IL(40), and c) photopolymerized Vc12/IL(40) at ambient temperature. The insets magnify selected regions. Corresponding POM textures under crossed polarizers (white arrows indicate the directions) are displayed in the upper panels.

structure (Figure 2a). The intercolumnar distance is estimated to be 5.6 nm. As the IL is introduced, there is a gradual decrease in the phase transition temperature from $Col_h$ to isotropic liquid (Iso) states. Eventually, when the IL content reaches 40 mol%, the $Col_h$ phase undergoes a transformation into the $Cub_M$ structure. Notably, the POM texture of the $Cub_M$ phase exhibits no birefringence (Figure 2b, upper panel), and these $Cub_M$ samples display higher viscosity compared to the $Col_h$ samples (Figure S3, Supporting Information). The transition from $Col_h$ to $Cub_M$ structure is primarily induced by the expanded rearrangement of ionophilic moieties within the LC systems. The lattice parameters of $Cub_M$ structure are determined from SAXS profile (Figure 2b). Three obvious scattering at $q$ = 1.03, 1.16, and 1.27 $nm^{-1}$, and tiny peaks at $q$ = 1.65, 1.92, and 2.13 $nm^{-1}$ are observed. The reciprocal spacing ratio of these peaks can be speculated to $\sqrt{4}:\sqrt{5}:\sqrt{6}:\sqrt{10}:\sqrt{14}:\sqrt{16}$, corresponding to the (200), (210), (211), (310), (321), and (400) diffractions of the $Cub_M$ phase with $Pm\bar{3}n$ symmetry.[28]

The mixtures of Vc12 and IL (Vc12/IL(x), where x denotes the mol% of IL) containing a 0.1 wt% photo-initiator can be polymerized upon exposure to UV light (350 nm; 5 mW $cm^{-1}$). The polymerization conversion of the vinyl imidazolium group was primarily assessed by using FTIR spectroscopy. The characteristic peak of the vinyl C-H stretching vibration at 3016 or 3014 $cm^{-1}$ is hardly observed (Figure S4, Supporting Information). However, the isolated C = C stretching vibration peak around 1653 $cm^{-1}$ is weakened. The free-standing LC films retaining $Col_h$ and $Cub_M$ nanostructures could be easily peeled off from the substrates. SAXS pattern for the photocured $Col_h$ LC film of Vc12/IL(30) ($P_{Col}$/IL(30)) observes the presence of intense $d_{100}$, $d_{110}$, and $d_{200}$ peaks (Figure S5a, Supporting Information). This result supported the maintenance of $Col_h$ ordering in the membrane with an intracolumnar distance of about 5.7 nm.

In addition, the photocured $Cub_M$ LC film of Vc12/IL(40), denoted as $P_{Cub}$/IL(40), shows clear diffraction peaks from $d_{200}$, $d_{210}$, and $d_{211}$ planes (Figure 2c). The optically transparent $Cub_M$ LC film exhibits excellent ionic conductivity at room temperature (**Figure 3**). For example, $P_{Col}$/IL(30) film shows approximately an order of magnitude higher ionic conductivity than the $P_{Col}$/IL(0) film. However, despite the $P_{Cub}$/IL(40) film having only a 10 mol% difference in IL content compared to $P_{Col}$/IL(30) film, its ionic conductivity is greatly enhanced, increasing from $1.6 \times 10^{-6}$ to $4.8 \times 10^{-5}$ S $cm^{-1}$. Activation energies were calculated as 74, 59, and 35 kJ $mol^{-1}$ for $P_{Col}$/IL(0), $P_{Col}$/IL(30), and $P_{Cub}$/IL(40) electrolyte films, respectively. This significant improvement in ionic conductivity was mainly attributed to the ordered micellar arrangement and greater IL confinement within the membrane. DSC thermograms show glass transition temperature ($T_g$) shifting from –14 to –31 °C with increasing IL contents (Figure S6, Supporting Information).

We demonstrate the bending actuation of a $P_{Cub}$/IL(40)-based actuator. This actuator was fabricated using the $Cub_M$ LC membrane sandwiched between two sheets of conductive PEDOT:PSS electrodes. Upon the application of voltage, ions can migrate along the ionophobic spherical surface with minimal energy barrier and then aggregate at the electrode interface to induce

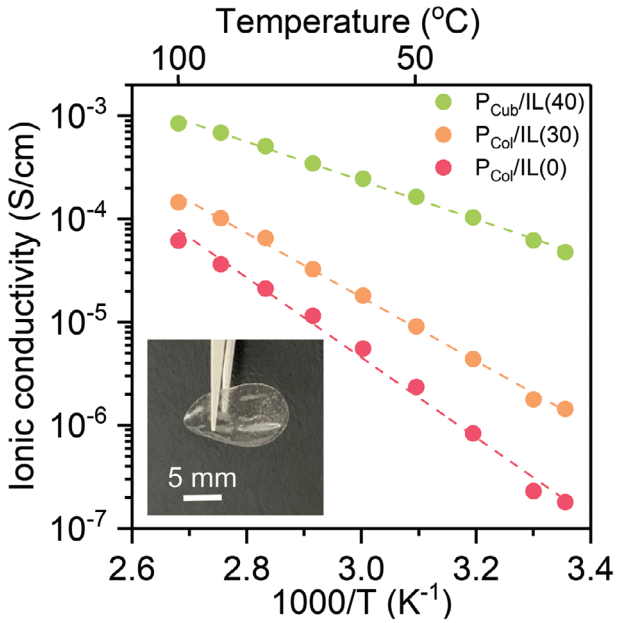


**Figure 3.** Ionic conductivities of $P_{Col}$/IL(0), $P_{Col}$/IL(30), and $P_{Cub}$/IL(40) films. The dash lines are fitted by the Arrhenius equation to the data. The inset photograph shows the $P_{Cub}$/IL(40) film.

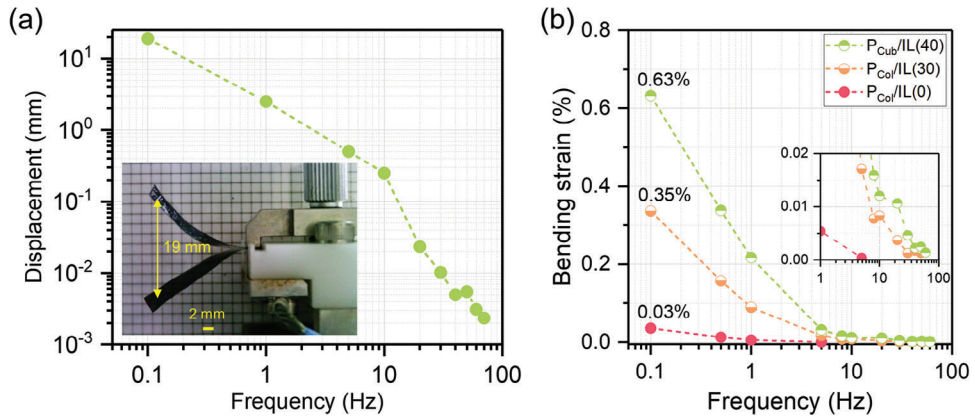


**Figure 4.** a) Bending displacement of $P_{Cub}$/IL(40)-based actuator with various frequencies. The inset shows the actuation appearance of $P_{Cub}$/IL(40)-based actuator under 2 V, 0.1 Hz. b) Frequency dependence of the bending strain of the $P_{Col}$/IL(0), $P_{Col}$/IL(30), and $P_{Cub}$/IL(40)-based actuators under an AC voltage of 2 V.

material bending. This behavior is attributed to the high ionic conductivity and low activation energy of continuous ionic pathways within the $Cub_M$ LC structure. The $P_{Cub}$/IL(40)-based actuator achieves a maximum displacement of approximately 19 mm at 0.1 Hz under an alternating current (AC) of 2 V (**Figure** 4a). We have investigated the actuators prepared by photo-crosslinked LC membranes having 3D interconnected $Col_h$ and $Cub_M$ nanostructures, respectively, while the ion was able to shuttle inside the 3D ionic pathways. The frequency-dependent bending strain is presented in Figure 4b, highlighting the superior performance of the $P_{Cub}$/IL(40)-based actuator, which exhibits a bending strain of 0.63%, in contrast to the 0.35% observed for the $P_{Col}$/IL(30)-based actuator under 2 V and 0.1 Hz. To gain insights into the bending actuation mechanism through ion accumulation at the electrode interface, cyclic voltammetry (CV) measurements were conducted. Current flow within the $P_{Cub}$/IL(40) and $P_{Col}$/IL(30)-based actuators exhibits the electric double layer capacitance behavior at a potential window of –1 V to 1 V (Figure S7a, Supporting Information). The $P_{Cub}$/IL(40)-based actuator demonstrates a specific capacitance of approximately 17.9 mF $cm^{-2}$ at a scan rate of 10 mV $s^{-1}$, while the $P_{Col}$/IL(30)-based actuator records 15.1 mF $cm^{-2}$ (Figure S7b, Supporting Information). This minor difference between the two actuators can be attributed to variations in ion content within the electrolyte layer, despite their distinct nanostructures.

As the response frequency increases, the bending strain of the actuators decreases. The $P_{Cub}$/IL(40)-based actuator achieves a maximum response frequency of up to 70 Hz. Our LC actuators exhibit exceptional high-frequency oscillation capabilities in comparison to other actuators constructed from block copolymer and amorphous polymer electrolyte materials.[9,29–32] Notably, it is worth highlighting that the $P_{Cub}$/IL(40) membrane contains only 13.3 wt% ionic liquid, significantly lower than reported high-performance actuators.[26,27]

Furthermore, we found the $P_{Col}$/IL(0)-based actuator without IL was still capable of inducing a slight deflection with a strain of 0.03% at 2 V and 0.1 Hz. This behavior primarily arises from the motion of anions within the polarization of the LC network. The bending response induced solely by anions illustrated minimal current generation within the actuator, in stark contrast to the $P_{Col}$/IL(30) and $P_{Cub}$/IL(40)-based actuators. These results underscore the pivotal role of ionic liquid in the polarized LC network, with even small IL quantities facilitating robust performance, likely attributed to the establishment of 3D ion pathways.

In addition, both $P_{Col}$/IL(30) and $P_{Cub}$/IL(40)-based actuators can be effectively operated at a low voltage of AC 0.5 and 1 V (Figure S8a, Supporting Information). Furthermore, the $P_{Cub}$/IL(40)-based actuator exhibits exceptional long-term durability, enduring over 10,000 cycles under 2 V and 1 Hz (Figure S8b, Supporting Information). The results support the idea that the LC electrolyte membrane with a micellar cubic structure can effectively and stably transport ions under a voltage supply.

We also assessed the generation force of the bending actuators for future application in soft robots. Under an AC voltage of 2 V at 0.1 Hz, the $P_{Cub}$/IL(40)-based actuator exhibited an impressive blocking force of 2.7 mN at the tip, estimated to be about 60 times its own weight. In contrast, the $P_{Col}$/IL(30)-based actuator yielded only 0.96 mN under identical conditions (**Figure** 5a). The notable difference in generation force between $P_{Col}$/IL(30)-based actuator and $P_{Cub}$/IL(40)-based actuator can be attributed to the moment of inertia resulting from the deformation of the actuators and their intrinsic elastic modulus.

From the perspective of the inertia moment, the $P_{Cub}$/IL(40)-based actuator possesses a larger moment of inertia than the $P_{Col}$/IL(30)-based actuator due to its superior bending motion. Consequently, the $P_{Cub}$/IL(40)-based actuator exhibits a higher bending speed, contributing to enhanced kinetic energy. On the other hand, we evaluated their Young's moduli by tensile test (Figure 5b). The tensile strain-stress curves exhibit a similar trend for both assembled actuators, composed of $P_{Col}$/IL(30) and $P_{Cub}$/IL(40) electrolytes, along with a pair of PEDOT:PSS electrodes, respectively. As a result, Young's modulus obtained from the slope in the initial curve within the 0.5% strain was estimated to be 409 MPa for $P_{Col}$/IL(30)-based actuators and 466 MPa for $P_{Cub}$/IL(40)-based actuators. While variations in the thickness of PEDOT:PSS electrodes might contribute to some differences in mechanical properties, the overall elasticity of the actuator predominantly depends on the electrolyte layer under identical thickness conditions. The enhanced elasticity of the $P_{Cub}$/IL(40) electrolyte can be attributed to the densely packed micellar spherical

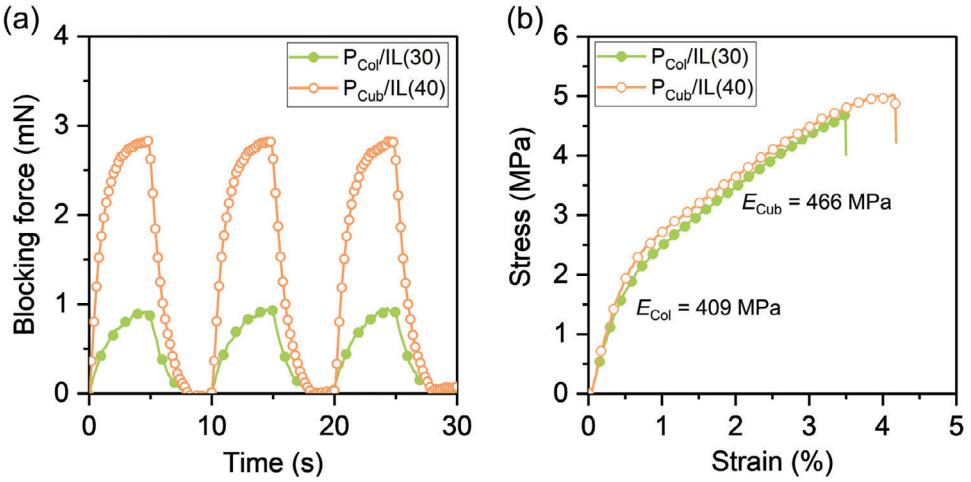


**Figure 5.** a) Generation force from bending actuators based on $P_{Col}$/IL(30) and $P_{Cub}$/IL(40) electrolytes, respectively, under an AC voltage of 2 V at 0.1 Hz. b) Tensile stress-strain curves of $P_{Col}$/IL(30) and $P_{Cub}$/IL(40)-based actuators.

structure in a unit space. This characteristic is further supported by the higher storage modulus (G') observed in the rheological measurements of the monomeric mixtures (Figure S3, Supporting Information). In contrast, $P_{Col}$/IL(30) electrolytes with randomly oriented LC columns may have free space between each LC column, resulting in lower mechanical properties compared to the $P_{Cub}$/IL(40) electrolyte.

The $Cub_M$ LC electrolyte, with its high viscoelastic framework and 3D ion pathway network, has enabled the development of a novel iEAP actuator capable of achieving high deformation and generating substantial force. To assess the advantages of this $Cub_M$ electrolyte, we compared it with a commercial polyvinylidene fluoride (PVdF) electrolyte containing over 30 wt% IL, sandwiched between PEDOT:PSS electrodes, as a control experiment. The actuator's dimensions are 20 mm in length, 10 mm in width, and 300 μm in thickness. While the conventional PVdF electrolyte actuator shows commendable performance, it cannot support heavy objects (**Figure 6a** and Movie S1, Supporting Information). In contrast, the flexible $P_{Cub}$/IL(40)-based actuator exhibits remarkable force generation, supporting a 4.0 g aluminum weight (equivalent to four 1 yen coins) in equilibrium under a 2 V DC voltage. Notably, the weight of the aluminum coins is over 65 times greater than that of the actuators. While it is possible to achieve impressive generation forces by stacking multiple layers of electrolytes to fabricate an actuator, this approach often comes at the cost of sacrificing the intrinsic benefits of flexibility and high bending displacement. Additionally, it can result in increased electric resistance between each electrolyte interface. Thanks to the ingenious design principle of a tough cubic LC electrolyte, we were able to harness the unique advantages of a single-layer membrane electrolyte, including flexibility, mechanical strength, high blocking force, and excellent bending capabilities in the actuator.

Furthermore, we demonstrated the effectiveness of an electronic pincer constructed from two sheets of $P_{Cub}$/IL(40)-based actuators. Despite their lightweight nature, these actuators exhibited remarkable bending performance, allowing them to securely grasp a styrofoam block (Figure 6b). Consequently, our newly designed cubic LC electrolytes can simultaneously facilitate efficient physical elastic deformation and ion transport, making them exceptionally well-suited for soft actuator applications. In our study, iEAP actuators fabricated using the novel $Cub_M$ LC electrolyte exhibit remarkable performance even at low ionic liquid concentrations, surpassing the bending performance of previously reported actuators (Figure 6c).

## 3. Conclusion

In conclusion, we have presented a novel LC molecular design aimed at creating well-defined micellar cubic LC electrolytes with continuous ion pathways. This approach primarily involves the supramolecular assembly of taper-shaped LC molecules, surrounded by IL, into stable spherical structures that remain intact over a wide temperature range. The transition from the original $Col_h$ structure to the $Cub_M$ structure is facilitated by the addition of IL, which not only impacts the structural arrangement but also influences the mechanical properties. The cubic structure combines the advantages of low tortuosity in ion diffusion pathways and densely packed ordered molecular spheres, resulting in multifunctional materials. The resultant $Cub_M$ electrolyte membrane preserves the benefits of being mechanically robust with interconnected ion pathways, enabling rapid and efficient ion diffusion. The tri-layer actuator, composed of the $Cub_M$ electrolyte and a pair of PEDOT:PSS electrodes, exhibits outstanding actuation performance under a low driven voltage of 2 V and 0.1 Hz. This includes a high bending strain (0.63%) and a high force generation (2.7 mN) at the tip of actuator, which enables it to lift heavy objects of 4 g. The design concept based on the construction of a periodic LC cubic structure represents a significant milestone in the development of new energy storage and transduction actuators.

## 4. Experiment Section

*General Preparation Methods*: Synthesis of ionic LC monomer (Vc12) and fabrication of PEDOT:PSS films and actuators are described in the Supporting Information.

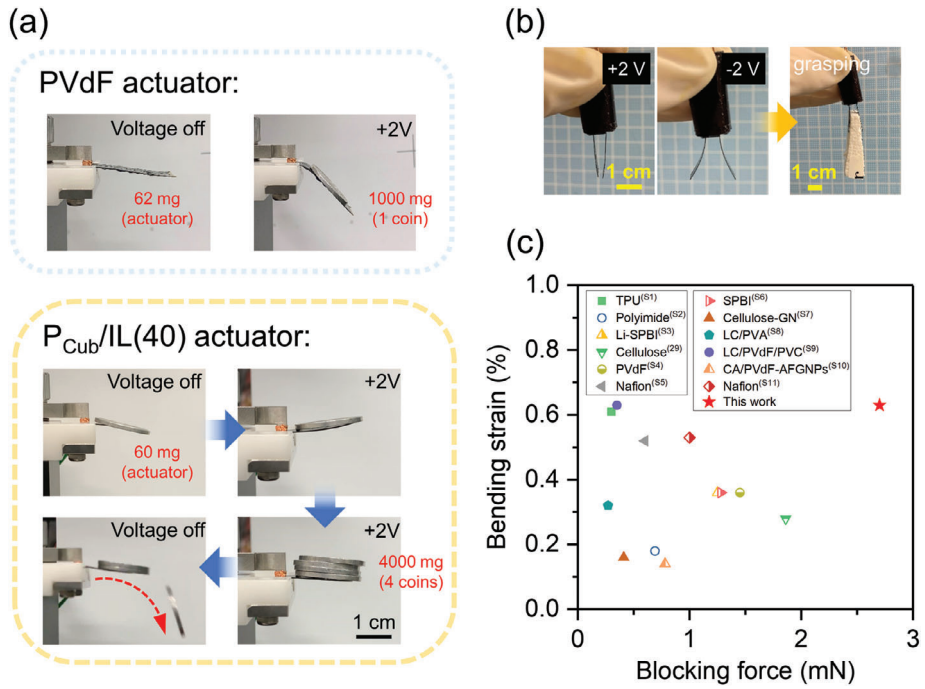


**Figure 6.** a) The comparison between a control 300 µm thick-actuator made of PVdF polymer electrolyte containing 30 wt% IL and PEDOT:PSS electrodes, which cannot support a 1 yen coin, and our P$_{Cub}$/IL(40)-based actuator of the same thickness, capable of carrying four 1 yen coins, equivalent to 4 g. b) An electronic pincer, constructed from two actuator sheets, securely holds a 150 mg styrofoam block by bending inward. c) The relationship between peak-to-peak bending strain and blocking force for the P$_{Cub}$/IL(40) actuator and other previously reported actuators. The detailed data can be found in Table S2 (Supporting Information).

*General Analysis Methods*: Polarized optical microscopy (POM) observations were performed using an Olympus BX51N-31P-O3 microscope equipped with a DP22 digital camera and a temperature control system (LINKAM T95-HS, LTS420E). Differential scanning calorimetry (DSC) measurements were carried out under a continuous argon purge (40 mL min$^{-1}$) using a NETZSCH DSC-3500 Sirius instrument connected with a liquid nitrogen cryo-system. The heating and cooling scan rates were 10 °C min$^{-1}$. Small-angle X-ray scattering (SAXS) measurements were performed by using Anton Paar SAXSess mc$^2$ instruments. Tensile tests were performed with a Shimadzu EZ-S setup at a stretching speed of 10 mm min$^{-1}$. Rheological measurements were performed using an Anton Paar MCR 102 rheometer (Anton Paar, Austria). A parallel plate geometry with an 8 mm diameter plate and a gap spacing of 0.3 mm was used for all the measurements. The measurements were conducted at an angular frequency of 10 rad s$^{-1}$ and a shear strain amplitude of 0.01–1000%.

*Cyclic Voltammetry Measurements*: CV measurements were carried out using an electrochemical analyzer (model 611E, CH Instruments) in a potential range of 1 to −1 V at scan rates varying from 10 to 50 mV s$^{-1}$. The specific capacitance (C$_{sc}$) was calculated via the following equation: $C_{sc} = \frac{\int_{V_1}^{V_2} i\,dV}{A(V_2 - V_1)\nu}$, where $i$ is the instant current (A), $A$ is the surface area of the electrode (cm$^2$), $\nu$ is the scan rate (V s$^{-1}$), $V_2$ and $V_1$ are the high and low potential limits (V).

*Ionic Conductivity Measurements*: Alternating current impedance measurements were carried out using a Metrohm AUTOLAB PGSTAT128N impedance analyzer. The frequency range was $10^2$–$10^7$ Hz and the applied voltage was 0.6 V. The sample was sandwiched between a pair of indium tin oxide (ITO)-coated glass substrates using a 55 µm-thick polyimide tape spacer with a 3 mm-diameter hole. The alignment-dependent ionic conductivity was measured in a gap cell geometry using interdigitated gold electrodes. The temperature was controlled using a Linkam hot stage. The impedance data were recorded every 10 °C upon heating from 25 to 100 °C. They were fitted to the equivalent circuit consisting of a constant phase element and a parallel RC element. Ionic conductivity $\sigma$ (S cm$^{-1}$) was calculated as $\sigma = L/R_bA$, where $R_b$ is the bulk resistance (Ω), $L$ is the sample thickness (cm), and $A$ is the sample area (cm$^2$). The $R_b$ value was obtained from the intercept of a semicircle on the real axis of impedance in the Nyquist plots. Temperature-dependent ionic conductivities were fitted by the Arrhenius equation: $\sigma = \sigma_0\, e^{\left(\frac{-E_a}{RT}\right)}$, where $R = 8.314$ J K$^{-1}$ mol$^{-1}$ is the ideal gas constant, $E_a$ is the activation energy (J mol$^{-1}$), $T$ is the absolute temperature ($K$), and $\sigma_0$ is the pre-exponential factor (S cm$^{-1}$).

*Actuation Performance Test*: The actuator strip was clamped between two stainless-steel electrodes connected to a potentiostat (Hokuto Denko, HAL3001A). Symmetrical square-wave alternating voltages or direct voltage generated by a function generator (YOKOGAWA FG400 30 MHz) were controlled using the potentiostat and applied to the actuator. The bending displacement was measured using a laser meter (Keyence, LK-H050, and LK-HD500). The laser was irradiated perpendicular to the actuator surface at a distance of 7 mm from the electrode. The signals of voltage, current, and displacement were recorded in a digital data logger (HIOKI LR8880). The actuation was captured using a USB camera (Sanwa Supply, 400-CAM058). The blocking force was measured by the load sensor connected to a force detection monitor (KYOWA LTS-50GA/KYOWA WGA-680A). The bending strain (%) was calculated as $\varepsilon = 2\delta d \times 100/(\delta^2 + L^2)$, where $\delta$ is the peak-to-peak displacement, $d$ is the total thickness of the actuator, and $L$ is the free length of the actuator. The actuation tests were performed under an ambient atmosphere with an average relative humidity of (40 ± 5)%.

## Supporting Information

Supporting Information is available from the Wiley Online Library or from the author.

## Acknowledgements

This work was supported by JST, PRESTO (Grant Number JPMJPR23QB), JSPS KAKENHI (Grant Number 21H02021), and Iketani Science and Technology Foundation (no. 0351202-A). The authors thank Dr. Junko Aimi for assistance with the SAXS instrument.

## Conflict of Interest

The authors declare no conflict of interest.

## Author Contributions

M.Y. and C.H.W. contributed equally to this work and were designated as the co-first authors. Conceptualization, methodology, funding acquisition, project administration, and supervision were done by M.Y; Investigation, writing, review, and editing were done by M. Y., C.-H. W., and C. L.

## Data Availability Statement

The data that support the findings of this study are available from the corresponding author upon reasonable request.

## Keywords

cubic liquid crystals, ionic electroactive polymer actuators, ionic liquids, photopolymerization, self-assembly

Received: November 9, 2023
Revised: December 26, 2023
Published online: January 26, 2024

[1] H. Bai, S. Li, R. F. Shepherd, *Adv. Funct. Mater.* **2021**, *31*, 2009364.
[2] H. Ham, M. Park, T. Park, X. Gao, Y. L. Park, M. J. Park, *Adv. Mater. Technol.* **2023**, *8*, 2300070.
[3] Y. Lee, J. Y. Oh, W. Xu, O. Kim, T. R. Kim, J. Kang, Y. Kim, D. Son, J. B.-H. Tok, M. J. Park, Z. Bao, T. W. Lee, *Sci. Adv.* **2018**, *4*, eaat7387.
[4] L. Lu, J. Liu, Y. Hu, Y. Zhang, H. Randriamahazaka, W. Chen, *Adv. Mater.* **2012**, *24*, 4317.
[5] U. Raza, S. Oh, R. Tabassian, M. Mahato, H. V. Nguyen, I. K. Oh, *Sens. Actuators B* **2022**, *352*, 131006.
[6] L. Lu, W. Chen, *Adv. Mater.* **2010**, *22*, 3745.
[7] R. K. Cheedarala, J. H. Jeon, C. D. Kee, I. K. Oh, *Adv. Funct. Mater.* **2014**, *24*, 6005.
[8] D. M. Correia, L. C. Fernandes, N. Pereira, J. C. Barbosa, J. P. Serra, R. S. Pinto, C. M. Costa, S. Lanceros–Méndez, *Appl. Mater. Today* **2021**, *22*, 100928.
[9] S. Imaizumi, H. Kokubo, M. Watanabe, *Macromolecules* **2012**, *45*, 401.
[10] S. Imaizumi, Y. Kato, H. Kokubo, M. Watanabe, *J. Phys. Chem. B* **2012**, *116*, 5080.
[11] J. Song, B. K. Cho, *Chem. Commun.* **2012**, *48*, 6821.
[12] M. A. Alam, J. Motoyanagi, Y. Yamamoto, T. Fukushima, J. Kim, K. Kato, M. Takata, A. Saeki, S. Seki, S. Tagawa, T. Aida, *J. Am. Chem. Soc.* **2009**, *131*, 17722.
[13] T. Kobayashi, T. Ichikawa, T. Kato, H. Ohno, *Adv. Mater.* **2017**, *29*, 1604429.
[14] T. Matsumoto, T. Ichikawa, J. Sakuda, T. Kato, H. Ohno, *Bull. Chem. Soc. Jpn.* **2014**, *87*, 792.
[15] T. Ichikawa, M. Yoshio, A. Hamasaki, J. Kagimoto, H. Ohno, T. Kato, *J. Am. Chem. Soc.* **2011**, *133*, 2163.
[16] T. Ichikawa, M. Yoshio, S. Taguchi, J. Kagimoto, H. Ohno, T. Kato, *Chem. Sci.* **2001**, *3*, 2012.
[17] T. Kato, *Angew. Chem., Int. Ed.* **2010**, *49*, 7847.
[18] G. Montalvo, M. Valiente, E. Rodenas, *Langmuir* **1996**, *12*, 5202.
[19] M. Emo, M. J. Stébé, J. L. Blin, A. Pasc, *Soft Matter* **2013**, *9*, 2760.
[20] Jayaraman, M. K. M., *Langmuir* **2018**, *34*, 2290.
[21] L. Zhang, J. Lin, S. Lin, *Macromolecules* **2007**, *40*, 5582.
[22] N. J. W. Penfold, J. R. Lovett, P. Verstraete, J. Smets, S. P. Armes, *Polym. Chem.* **2017**, *8*, 272.
[23] F. Lv, Z. An, P. Wu, *Macromolecules* **2020**, *53*, 367.
[24] K. Yoshida, S. Tanaka, T. Yamamoto, K. Tajima, R. Borsali, T. Isono, T. Satoh, *Macromolecules* **2018**, *51*, 8870.
[25] C. H. Wu, W. Meng, M. Yoshio, *ACS Mater. Lett.* **2022**, *4*, 153.
[26] C. H. Wu, M. Yoshio, *J. Mater. Chem. C* **2023**, *11*, 10154.
[27] C. H. Wu, W. Meng, K. Iakoubovskii, M. Yoshio, *ACS Appl. Mater. Interfaces* **2023**, *15*, 4495.
[28] H. Dai, X. Yang, X. Tan, F. Su, X. Cheng, F. Liu, *Chem. Commun.* **2013**, *49*, 10617.
[29] F. Wang, Z. Jin, S. Zheng, H. Li, S. Cho, H. J. Kim, S. J. Kim, E. Choi, J. O. Park, S. Park, *Sens. Actuators B* **2017**, *250*, 402.
[30] C. Lu, Y. Yang, J. Wang, R. Fu, X. Zhao, L. Zhao, Y. Ming, Y. Hu, H. Lin, X. Tao, Y. Li, W. Chen, *Nat. Commun.* **2018**, *9*, 752.
[31] T. J. S. Kim, M. J. Park, *Nat. Commun.* **2013**, *4*, 2208.
[32] H. K. Kim, U. H. Choi, M. J. Park, *Nat. Commun.* **2016**, *7*, 13576.